Optomechanics in superfluid helium coupled to a fiber-based cavity

2017 J. Opt. 19 034001

(http://iopscience.iop.org/2040-8986/19/3/034001)

IOP Publishing Journal of Optics
J. Opt. 19 (2017) 034001 (14pp) https://doi.org/10.1088/2040-8986/aa551e

Optomechanics in superfluid helium coupled to a fiber-based cavity

A D Kashkanova[1,5], A B Shkarin[1], C D Brown[1], N E Flowers-Jacobs[1], L Childress[1,2], S W Hoch[1], L Hohmann[3], K Ott[3], J Reichel[3] and J G E Harris[1,4]

[1] Department of Physics, Yale University, New Haven, CT, 06511, United States of America
[2] Laboratoire Kastler Brossel, ENS/UPMC-Paris 6/CNRS, F-75005 Paris, France
[3] Department of Applied Physics, Yale University, New Haven, CT, 06511, United States of America
[4] Department of Physics, McGill University, 3600 Rue University, Montreal, Quebec H3A 2T8, Canada

E-mail: anna.kashkanova@yale.edu

Received 23 September 2016, revised 29 November 2016
Accepted for publication 21 December 2016
Published 1 February 2017

Abstract

Presented in this paper are measurements of an optomechanical device in which various acoustic modes of a sample of superfluid helium couple to a fiber-based optical cavity. In contrast with recent work on the paraxial acoustic mode confined by the cavity mirrors (Kashkanova *et al Nat. Phys.* 2016 (https://doi.org/10.1038/NPHYS3900)), we focus specifically on the acoustic modes associated with the helium surrounding the cavity. This paper provides a framework for understanding how the acoustic modes depend on device geometry. The acoustic modes are observed using the technique of optomechanically induced transparency/amplification. The optomechanical coupling to these modes is found to be predominantly photothermal.

Keywords: superfluid, liquid helium, optomechanics, fluid mechanics, optical cavities

(Some figures may appear in colour only in the online journal)

1. Introduction

Incorporating fluid into an optomechanical system can be beneficial in a number of ways. First, it can provide new avenues for studying the fluid's properties [2, 3]. Second, a fluid with high thermal conductivity can be used to thermalize a mechanical element, allowing higher optical powers to be used [4]. Third, a fluid can be used as a mechanical element, which simplifies the assembly process, as the fluid can conformally fill or coat an electromagnetic resonator [5, 6].

There are two distinct approaches to using fluid in an optomechanical system: immersing a solid resonator into fluid [6, 7], or filling a hollow resonator with fluid [1–3, 8]. If one wishes to perform experiments at cryogenic temperature (which is necessary to achieve quantum behavior in almost all optomechanical systems), liquid helium is the only choice of fluid, since it does not solidify under its own pressure. In addition it has a variety of useful properties for optomechanical applications, such as very low optical absorption [9], high thermal conductivity [10], and acoustic loss proportional to T^4 [11], which becomes low at dilution refrigerator temperatures.

In this paper we investigate the coupling between superfluid helium and a fiber-based optical cavity. In contrast with our previous work [1], we do not focus on the paraxial acoustic modes confined by the cavity mirrors and co-located with the optical modes, but rather study the lower frequency modes defined by the fibers and the surrounding components. We use the technique of optomechanically induced transparency/amplification (OMIT/OMIA) to measure the response of these modes to an optical drive. By comparing these measurements to a theoretical model similar to the one described in [1], we find that these modes' optomechanical coupling is partially electrostatic and partially photothermal. The photothermal coupling appears to result from two distinct mechanisms, one related to thermal transport within the superfluid and the other related to thermal expansion of the materials confining the superfluid. These results provide insight into the various mechanisms by which photothermal

[5] Author to whom any correspondence should be addressed.

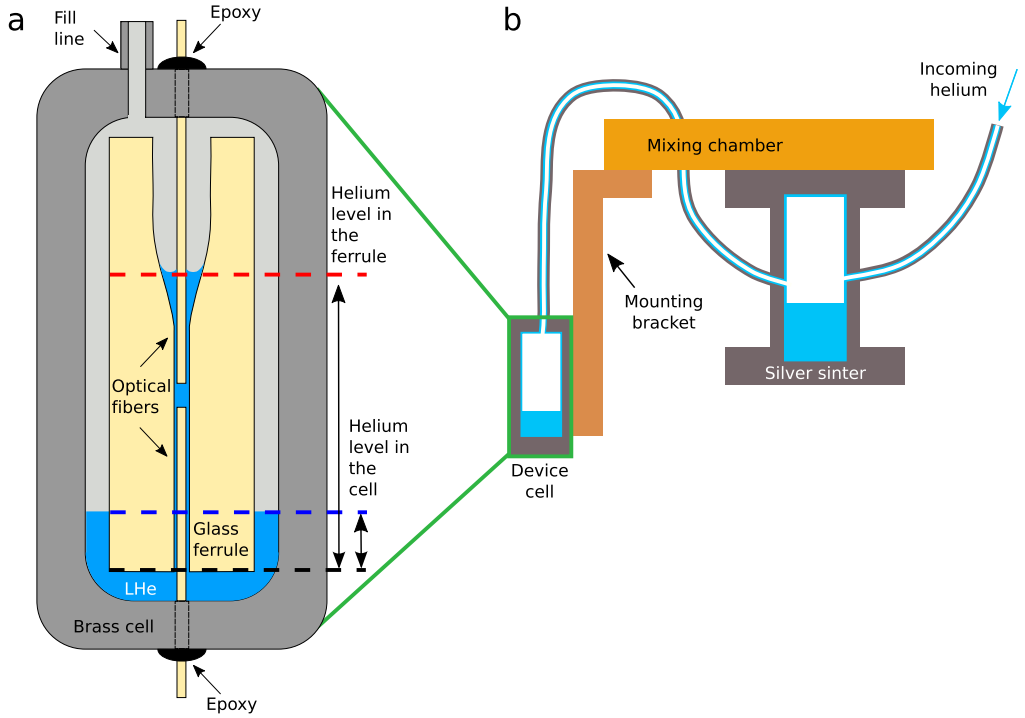

Figure 1. The experimental setup. (a) A schematic drawing of the device. The optical cavity is formed between two glass fibers (yellow), aligned in a glass ferrule (yellow). The ferrule is epoxied into a brass cell (gray). The optical fibers are epoxied to the brass cell as well, forming superfluid helium tight seals. The helium (blue) is delivered via the fill line shown at the top of the cell. The helium level in the cell is measured from the bottom of the ferrule (dashed black line) and is shown with a dashed blue line. The helium level in the ferrule is higher due to capillary action and is shown with a dashed red line. (b) A schematic drawing of the helium delivery system at the mixing chamber (MC) of the dilution refrigerator. The helium (blue) enters through a capillary (shown on the right). It first condenses in a silver sinter (gray), and then flows via Rollin film into the cell. The cell is attached to a gold-plated OFHC copper mounting bracket, which is attached to the MC.

processes can lead to optomechanical coupling. They are also important for characterizing superfluid-filled optical cavities.

2. Methods

The device, shown schematically in the figure 1(a), is located in a cell made of brass. A glass ferrule with 133 ± 5 μm diameter bore is epoxied inside the cell. The bore is funneled on one end. An optical cavity is created by inserting a pair of 125 μm diameter fibers into the bore [12]. Each fiber face (the cleaved end of the fiber) has an indentation created by CO_2 laser ablation [13, 14]. The depth of the indentation is $\simeq$1.5 μm and the radii of curvature are: $R_1 = 282$ μm and $R_2 = 409$ μm. On each fiber end, a distributed Bragg reflector optical coating has been deposited [15]. The optical transmission is 103 ppm for the input mirror and 10 ppm for the back mirror, which results in a single sided cavity. The mirror separation is $L = 84$ μm and the optical cavity linewidth is $\kappa = 2\pi \times 54$ MHz. The input coupling is $\kappa_{\rm in} = 2\pi \times 27$ MHz.

The mounting of the cell is shown in figure 1(b). The cell is mounted to the mixing chamber (MC) of a dilution refrigerator, which is kept at temperature $T < 100$ mK. The cell is filled through a 1.5 mm outer diameter (500 μm inner diameter) stainless steel capillary. The capillary is wound around copper bobbins at each stage of the refrigerator for thermalization. At the MC, there is a sintered silver heat exchanger which is used to thermalize the incoming helium to the MC temperature.

The device is filled by adding small doses of helium. The time when the dose is added and the amount of helium in each dose are recorded. Using this information, the level of helium in the cell can be calculated, as described in section 2.1.

The resonant frequency of the optical cavity is monitored in order to determine when the cavity is filled. Filling the cavity changes its effective length by a factor of 1.028 (the index of refraction of LHe) [16], changing the frequency of the cavity modes correspondingly. Once the cavity is filled, the optomechanically induced transparency (OMIT) [17] is used to observe the acoustic modes. Using this technique, two distinct families of acoustic modes are observed: low frequency modes (20−300 KHz) and high frequency modes (2 −20 MHz). Some of the low frequency modes show strong dependence on the helium level, from which we conclude that the mode profiles extend beyond the cavity volume into the helium sheath between the fiber and the ferrule, and into the funnel. Those modes are referred to as ‘ferrule modes’. In contrast, the high frequency modes are independent of the helium level and have frequencies consistent with the radial acoustic modes of a cylinder of helium. Those modes are referred to as ‘radial modes’.

2.1. Filling the device

As described above, helium is added to the cell in discrete doses. Each dose at room temperature contains $\simeq 13.4$ cm^3 helium gas at a pressure of $\simeq 1100$ mbar. The doses are added at a rate of approximately one every three minutes. The doses are first released into a liquid nitrogen cold trap, then, after one minute, are added to the cell. Due to the geometry of the system (shown in figure 1(b)), helium first condenses inside the volume containing the sintered silver heat exchanger (which is a local gravitational minimum), and then 'creeps' as a Rollin film [18] along the walls of a connecting capillary to fill the cell. The film thickness d is given by [19]: $d = \eta h^{-1/3}$. Here $\eta = 6.5 \times 10^{-9}$ m$^{4/3}$ and h is the height above the helium level. Before helium starts to condense in the cell, all parts of the system (the sintered silver heat exchanger, the cell, the capillary connecting the sintered silver heat exchanger to the cell) need to be covered by the superfluid Rollin film. The surface area of the sintered silver heat exchanger is specified to be $\simeq 10$ m^2 [20] which is at least two orders of magnitude larger than combined surface area of other parts of the system. The volume of liquid helium necessary to cover the sintered silver heat exchanger with the Rollin film is estimated to be 0.16 cm$^3 < V_{\rm film} < 0.38$ cm^3. Both upper and lower bounds are found by assuming constant film thickness throughout the sinter. The lower bound results from assuming the bulk helium level to be located in the device (6 cm below the top of the sinter), while the upper bound results from assuming the bulk helium level to be located in the volume containing the sinter (0.5 cm below the bottom of the sinter).

As soon as the amount of helium in the system exceeds $V_{\rm film}$, helium starts condensing at the bottom of the volume containing the sintered silver heat exchanger and starts flowing into the cell at a rate $\dot{V}$ [19]:

$$\dot{V} = 2\pi R_{\rm c} d_{\rm thin} v_{\rm crit}. \tag{1}$$

Here, $R_{\rm c}$ is the inner radius of the capillary, $d_{\rm thin}$ is the film thickness at its thinnest point, and $v_{\rm crit} \simeq 30$ cm s^{-1} is the critical superfluid film velocity [19]. The highest point of the capillary is located $\simeq 20$ cm above the minimum liquid level in the sinter, resulting in the minimum film thickness $\simeq 14$ nm. Therefore the rate of filling the device is $\dot{V} = 4 \times 10^{-4}$ cm^3 min^{-1}. If, at any point, there is no helium accumulated at the bottom of the sintered silver heat exchanger volume, helium stops flowing into the device.

Using this model, we can describe the volume of liquid helium accumulated in the device as a function of time. Using a CAD model of the cell, the helium level in the cell can be modeled as a function of the volume of helium accumulated in the device. This is shown with a blue line on figure 2(a).

2.2. Capillary action

Since the cavity is located inside the ferrule, the helium level in the ferrule is of interest. The helium level in the ferrule is higher than the helium level in the cell due to capillary action [21]. In what follows, we calculate the helium level in the ferrule as a function of the helium level in the cell.

2.2.1. Hollow tube of constant radius. To understand capillary action in the ferrule, consider first a simple model: a thin tube of radius r submerged in a fluid bath. Assume that the pressure above the bath is zero. The surface tension is σ and the contact angle is θ_c, as shown in the inset of the figure 2(b). The height h^* to which the fluid rises can be determined by balancing gravitational potential energy and interfacial energy, which is done done by minimizing the free energy. The free energy of the system is given by:

$$F(h) = \int_V \rho g z \mathrm{d}V - \int_A \sigma \cos\theta_c \mathrm{d}A. \tag{2}$$

Here V is the volume of the fluid in the capillary above the bath level, and A is the area over which helium is in contact with glass above the bath level. The values ρ and g are the density of the fluid and the gravitational constant. In the case above, ignoring the meniscus, we arrive at the equation:

$$\begin{aligned} F(h) &= \rho g \pi r^2 \int_0^h z \mathrm{d}z - \sigma \cos\theta_c 2\pi r h \\ &= \rho g \pi r^2 \frac{h^2}{2} - \sigma \cos\theta_c 2\pi r h. \end{aligned} \tag{3}$$

The height of the fluid in the capillary is then:

$$h^* = \frac{2\sigma \cos\theta_c}{\rho g r}. \tag{4}$$

For a 133 μm diameter capillary submerged in superfluid helium ($\rho = 145$ kg m^{-3} [16], $\theta_c = 0°$ [22] and $\sigma = 3.78 \times 10^{-4}$ J m^{-2} [22], the fluid rises by $h^* = 8$ mm.

2.2.2. Hollow axissymmetric tube of arbitrary shape. The ferrule is a hollow axissymmetric tube of arbitrary shape: $r = r(z)$. Here r is the distance from the axis of the ferrule and z is the distance from the bottom of the ferrule. The free energy is:

$$\begin{aligned} F(h) = \rho g \pi \int_0^h r(z)^2 z \mathrm{d}z - \sigma \cos\theta_c 2\pi \\ \times \int_0^h r(z) \sqrt{1 + \left(\frac{\mathrm{d}r}{\mathrm{d}z}\Big|_z \right)^2} \mathrm{d}z. \end{aligned} \tag{5}$$

In addition, there is a fiber in the center of the ferrule, which is modeled as a solid cylinder of constant radius $r_{\rm fib}$. The free energy then is:

$$\begin{aligned} F(h) = \rho g \pi \int_0^h [r(z)^2 z - r_{\rm fib}^2 z] \mathrm{d}z \\ - \sigma \cos\theta_c 2\pi \int_0^h \left[r(z) \sqrt{1 + \left(\frac{\mathrm{d}r}{\mathrm{d}z}\Big|_z \right)^2} + r_{\rm fib} \right] \mathrm{d}z. \end{aligned} \tag{6}$$

The derivative of the free energy with respect to h, evaluated at h^* is:

$$\begin{aligned} \frac{\mathrm{d}F}{\mathrm{d}h}\Big|_{h^*} = \rho g \pi [r(h^*)^2 - r_{\rm fib}^2] h^* \\ - \sigma \cos\theta_c 2\pi \left[r(h^*) \sqrt{1 + \left(\frac{\mathrm{d}r}{\mathrm{d}z}\Big|_{h^*} \right)^2} + r_{\rm fib} \right] = 0. \end{aligned} \tag{7}$$

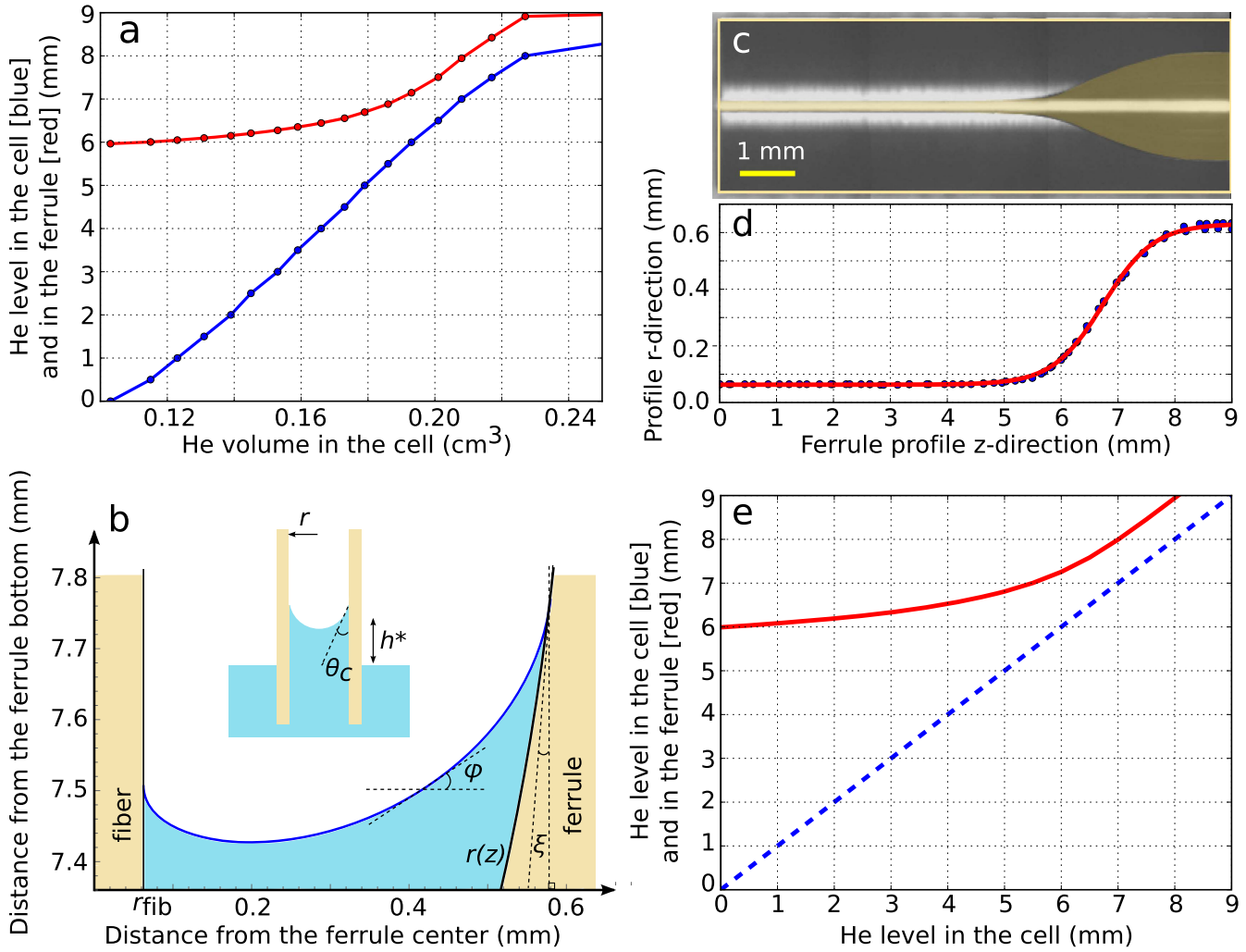

Figure 2. Helium level in the ferrule. (a) Helium level in the cell (blue) and in the ferrule (red) as a function of the volume of helium accumulated in the device (blue). Zero on the vertical axis corresponds to the bottom of the ferrule. As more helium is added to the cell, the helium level in the cell changes nonlinearly, due to cell geometry. A CAD model of the cell geometry was used to calculate helium level inside the cell, given the volume of added helium. Helium level in the ferrule was calculated using the blue points and the results from panel (e). (b) Inset: A schematic drawing of a cylindrical capillary (yellow) of radius r, submerged in liquid. The contact angle is θ. Due to capillary action the liquid rises to height h^*. Main figure: A plot of the superfluid helium meniscus (blue) formed in the space between the fiber (yellow) and the ferrule (yellow), calculated using the procedure described in section 2.2. The fiber has constant radius $r_{\rm fib}$. The ferrule profile is described by $r(z)$. The ferrule profile makes an angle $\xi(z)$ with the vertical. The angle ϕ is the slope angle of the liquid. (c) A photograph of the ferrule. Yellow shading indicates the funnel and the bore. (d) The ferrule profile extracted from the photograph (c) is shown using blue dots. The red line is a fit of equation (8) to the profile. (e) The helium level in the ferrule plotted as a function of helium level in the cell (red solid line). The blue dashed line illustrates unity slope. As soon as helium touches the bottom of the ferrule, it gets sucked in by the capillary action to a height of 6 mm, which is where the bore starts to widen into the funnel.

Equation (7) can be used to find the height of the capillary rise for the ferrule with a fiber, provided the ferrule profile is known.

A photo of the ferrule is shown in the figure 2(c). The ferrule is made of borosilicate glass with index of refraction $n = 1.52$. The length and diameter of the ferrule are 9 mm and 3 mm respectively. This information can be used to correct the image and extract the profile of the ferrule bore. The extracted profile is shown in figure 2(d) with blue circles. In order to evaluate equation (7) analytically, the profile is fit to the function:

$$r(z) = A\tanh\left(\frac{x-B}{C}\right) + D. \tag{8}$$

The following values are found for the fit parameters: $A = 284$ μm, $B = 6739.5$ μm, $C = 890.4$ μm, $D = 347$ μm. The fit is shown in figure 2(d) with a red line.

In addition, helium forms a meniscus in the ferrule, which is shown in figure 2(b). Its shape is calculated following [23]. The shape of the interface is described in parametric form by the slope angle ϕ:

$$r = R(\phi), \qquad z = Z(\phi). \tag{9}$$

Two differential equations describe the shape of the meniscus:

$$\frac{{\rm d}R(\phi)}{{\rm d}\phi} = \frac{\cos\phi}{Q(\phi)} \quad \text{and} \quad \frac{{\rm d}Z(\phi)}{{\rm d}\phi} = \frac{\sin\phi}{Q(\phi)}, \tag{10}$$

where $Q(\phi)$ is given by

$$Q(\phi) = \frac{Z(\phi)}{l^2} - \frac{\sin\phi}{R(\phi)}. \tag{11}$$

Here, l is the capillary length: $l = \sqrt{\sigma/\rho g}$. For a constant-radius hollow capillary, equations (10) are solved subject to the following boundary conditions:

$$R(0) = 0 \qquad \text{and} \qquad Z(0) = h_m^*. \tag{12}$$

Here, h_m^* is the height of the lowest point of the meniscus. The height h_m^* that satisfies the condition $R(\theta_c) = r$ is then found.

For the system used in the experiment (a ferrule whose profile is described by a function $r(z)$ with a fiber with radius r_{fib} in the center), the initial conditions become:

$$R(-\pi/2 + \theta_c) = r_{\text{fib}} \qquad \text{and} \qquad Z(-\pi/2 + \theta_c) = h_m^*, \tag{13}$$

h_m^* is then found to satisfy the two conditions below:

$$R(\pi/2 - \theta_c - \xi(z)) = r(Z(\pi/2 - \theta_c - \xi(z)))$$
$$\text{and} \qquad \arctan(r'(Z(\pi/2 - \theta_c - \xi(z)))) = \xi(z). \tag{14}$$

Here, $\xi(z)$ is the angle of the ferrule profile, as shown in figure 2(b). The solution to equation (7) is used an the initial guess for h_m^*.

The helium level in the ferrule, calculated using the procedure outlined above, is shown in figure 2(e) with a red line. The blue dashed line is a line with unity slope. From figure 2(e) it is clear that as soon as superfluid helium reaches the bottom of the ferrule, the helium level inside of the ferrule goes up to 6 mm, filling the optical cavity and making it possible to observe the acoustic modes. The relationship between the helium level in the cell and helium level in the ferrule allows us to plot the helium level in the ferrule as a function of liquid helium volume in the cell (shown in figure 2(a) with a red line).

3. Mode shapes

3.1. Optical modes

The intensity of the TEM_{00} optical cavity mode employed in the experiment is approximately proportional to:

$$I(r, z) \propto \sin\left(\frac{2\pi z}{\lambda_{\text{opt}}}\right)^2 \text{e}^{-\frac{2r^2}{w^2}}. \tag{15}$$

Here $\lambda_{\text{opt}} = 1,504$ nm is the optical wavelength in liquid helium and $w \simeq 7$ μm is the mode field radius [24]. Since the indentations on the fiber faces are not always centered on the fibers, and the fibers are possibly not centered in the ferrule, the optical mode (confined by the indentations) can be slightly offset from the center of the radial acoustic mode (confined by the inner walls of the ferrule). Assuming the existence of such an offset, x_0, the intensity profile can be modeled in the following manner:

$$I(x, y, z) \propto \sin\left(\frac{2\pi z}{\lambda_{\text{opt}}}\right)^2 \text{e}^{-\frac{2((x-x_0)^2+y^2)}{w^2}}. \tag{16}$$

The offset of the indentation from the fiber centers was measured to be $x_0 \simeq 1$–3 μm.

3.2. Radial acoustic modes

The acoustic radial modes in the liquid helium can be modeled as solutions of the time independent wave equation in a cylinder of radius R with zero flux on all surfaces and with zero longitudinal number, that is independent of z [25]:

$$\phi_{mn}(r, \theta) = J_m(\alpha_{mn} r/R)\cos m\theta. \tag{17}$$

Here ϕ is the velocity potential, J_m is the mth Bessel function of the first kind, α_{mn} is the nth zero of the derivative of J_m. The frequencies of the modes are:

$$\omega_{mn} = \frac{v\alpha_{mn}}{R}. \tag{18}$$

The frequencies of the modes are shown in the figure 3(a) with red dashed lines ($m = 0$) and blue dashed lines ($m = 1$).

To check if deviations of the geometry from an ideal cylinder have noticeable effect, the frequencies of the radial modes are also calculated by using finite element modeling software (COMSOL) to solve the wave equation for a cylinder of helium with length $L = 84$ μm and radius $R = 67$ μm with the 1.5 μm deep indentations for the mirrors with appropriate radii of curvature. The wave equation is solved for both $m = 0$ and $m = 1$ cases. The boundary condition is 'zero flux' on all the boundaries. The frequencies obtained via COMSOL simulations are in good agreement with frequencies calculated for a perfect cylinder, as can be seen by comparing red ($m = 0$) and blue ($m = 1$) lines in the figure 3(b) with the corresponding lines found analytically and shown in figure 3(a). The profiles for some of the modes are shown in figure 3(c).

3.3. Ferrule acoustic modes

The frequencies of the ferrule modes are found by implementing the whole geometry of the ferrule, described by equation (8), fibers and meniscus in COMSOL and solving the wave equation for this geometry. All of the helium-glass boundaries are set to be 'zero flux' boundaries. The bottom end of the ferrule is open, so it requires zero-pressure boundary condition ('Dirichlet boundary condition') and the top surface of the helium (helium-vacuum boundary), which has the meniscus shape as shown in figure 2(b), is described by a 'free surface' boundary condition.

Since it was experimentally observed that the frequencies of some of the ferrule modes change with the level of helium, we simulate the mode frequencies versus the helium level in the ferrule. Figure 4(a) shows the profiles of the modes when the helium level in the ferrule is 6.8 mm. The solid lines in figure 4(b) show the mode frequencies obtained via COMSOL simulations for different volumes of helium accumulated

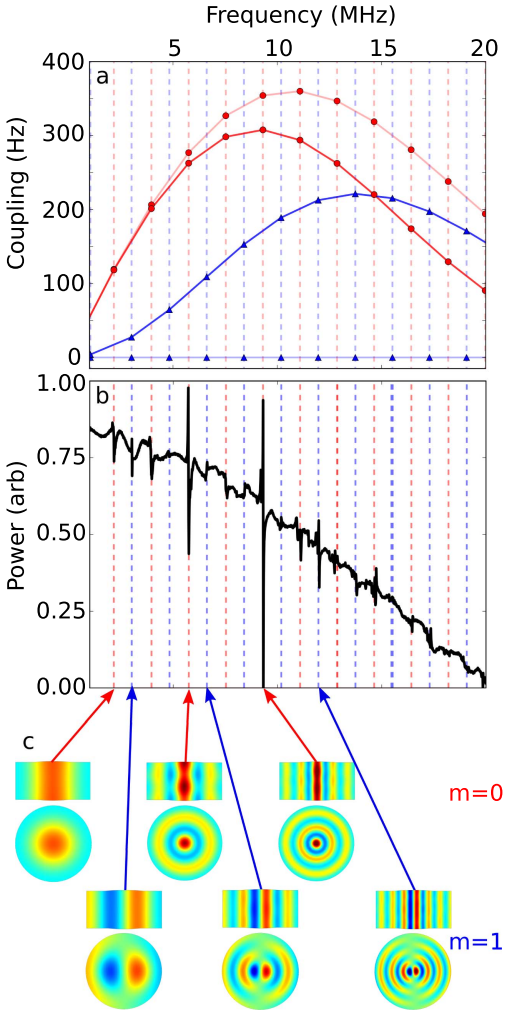

Figure 3. The radial modes. (a) The electrostrictive coupling rate g_0 to the radial modes of different frequencies. The red dashed and blue dashed vertical lines show the frequencies of the radial modes with $m = 0$ and $m = 1$ respectively, calculated using equation (18). The faint red (blue) line connecting the red circles (blue triangles) shows the coupling to $m = 0$ ($m = 1$) radial modes, calculated using methods in section 4, assuming the optical and acoustic modes are perfectly aligned. The bright red (blue) line connecting the red circles (blue triangles) shows the coupling to $m = 0$ ($m = 1$) radial modes, assuming the optical and acoustic modes are offset by 3 μm. The misalignment leads to decrease in coupling to $m = 0$ mode and to emergence of coupling to $m = 1$ mode. (b) The red dashed and blue dashed vertical lines show the frequencies of the radial modes with $m = 0$ and $m = 1$ respectively, found using COMSOL simulations. They match with the lines of panel (a), demonstrating that the deviations of the shape of the space between the fibers from the ideal cylinder do not influence the frequencies of the modes significantly. The OMIT/OMIA signal for the intracavity beatnote frequency in range 1–20 MHz is shown with a thick black line. The overall downward slope is due to the cavity filtering. The measured mode frequencies match well with the predicted frequencies for $m = 0$ and $m = 1$ modes. (c) The mode profiles for some of the modes, calculated using COMSOL.

in the device. The color of each line indicates the relative amount of energy stored in the sheath to the energy stored in the funnel. The modes with a large fraction of energy stored in the funnel show dependence on the helium level, decreasing in frequency as the helium level increases.

4. Electrostrictive coupling

In this section the electrostrictive coupling between the optical cavity and the acoustic modes of the liquid helium is described. The coupling arises because the effective cavity length depends on the density of helium that the optical mode overlaps with. Overlap with regions of higher helium density (higher index of refraction) increases the effective length and overlap with the regions of lower helium density (lower index of refraction) decreases the effective length. The expression for the electrostrictive coupling is derived as follows.

Changes in pressure in liquid helium can change the index of refraction locally as seen from the Clausius–Mossotti relation [26]:

$$\frac{n^2-1}{n^2+2} = \frac{4\pi\rho\alpha_{\mathrm{M}}}{3M}. \tag{19}$$

Here, n is the refractive index, ρ is the density, α_{M} is the molar polarizability and M is the molar mass. For $n = 1.028$, the left side of the equation is approximately $2(n-1)/3$, and hence $\rho \propto (n-1)$; therefore

$$\frac{\delta\rho}{\rho} = \frac{\delta n}{n-1}. \tag{20}$$

Given the spacial profile of the relative change in the refractive index $\delta n(\vec{r})$, we can find optomechanical coupling as:

$$g_0 = \omega_c \frac{\int_V I(\vec{r})\delta n(\vec{r})\mathrm{d}^3\vec{r}}{\int_V I(\vec{r}) n \mathrm{d}^3\vec{r}} = \omega_{\mathrm{c}}(n-1)\frac{\int_V I(\vec{r})\frac{\delta\rho(\vec{r})}{\rho}\mathrm{d}^3\vec{r}}{\int_V I(\vec{r}) n \mathrm{d}^3\vec{r}}. \tag{21}$$

Here $I(\vec{r})$ is the optical intensity profile and ω_{c} is the optical cavity resonant frequency. The relative change in density for a liquid is equivalent to strain $\epsilon(\vec{r})$. From the continuity equation the relative change in density is proportional to the velocity potential $\phi(\vec{r})$. Therefore we can express relative change in density as:

$$\frac{\delta\rho(\vec{r})}{\rho} \equiv \epsilon(\vec{r}) \equiv \epsilon_1 p(\vec{r}), \tag{22}$$

where ϵ_1 is a constant and $p(\vec{r})$ is a normalized mode profile. This leads to the following expression for g_0:

$$g_0 = \omega_{\mathrm{c}}(n-1)\epsilon_1 \frac{\int_V I(\vec{r}) p(\vec{r})\mathrm{d}^3\vec{r}}{\int_V I(\vec{r}) n \mathrm{d}^3\vec{r}}. \tag{23}$$

In the equation (23) the values for all quantities except for ϵ_1 are known. To find the value of ϵ_1, we write the energy stored in the fluctuations of the mode in terms of the elastic potential energy:

$$E_1 = \int_V \frac{1}{2} K\epsilon(\vec{r})^2 \mathrm{d}^3\vec{r} = \frac{1}{2} v^2 \rho \epsilon_1^2 \int_V p(\vec{r})^2 \mathrm{d}^3\vec{r}. \tag{24}$$

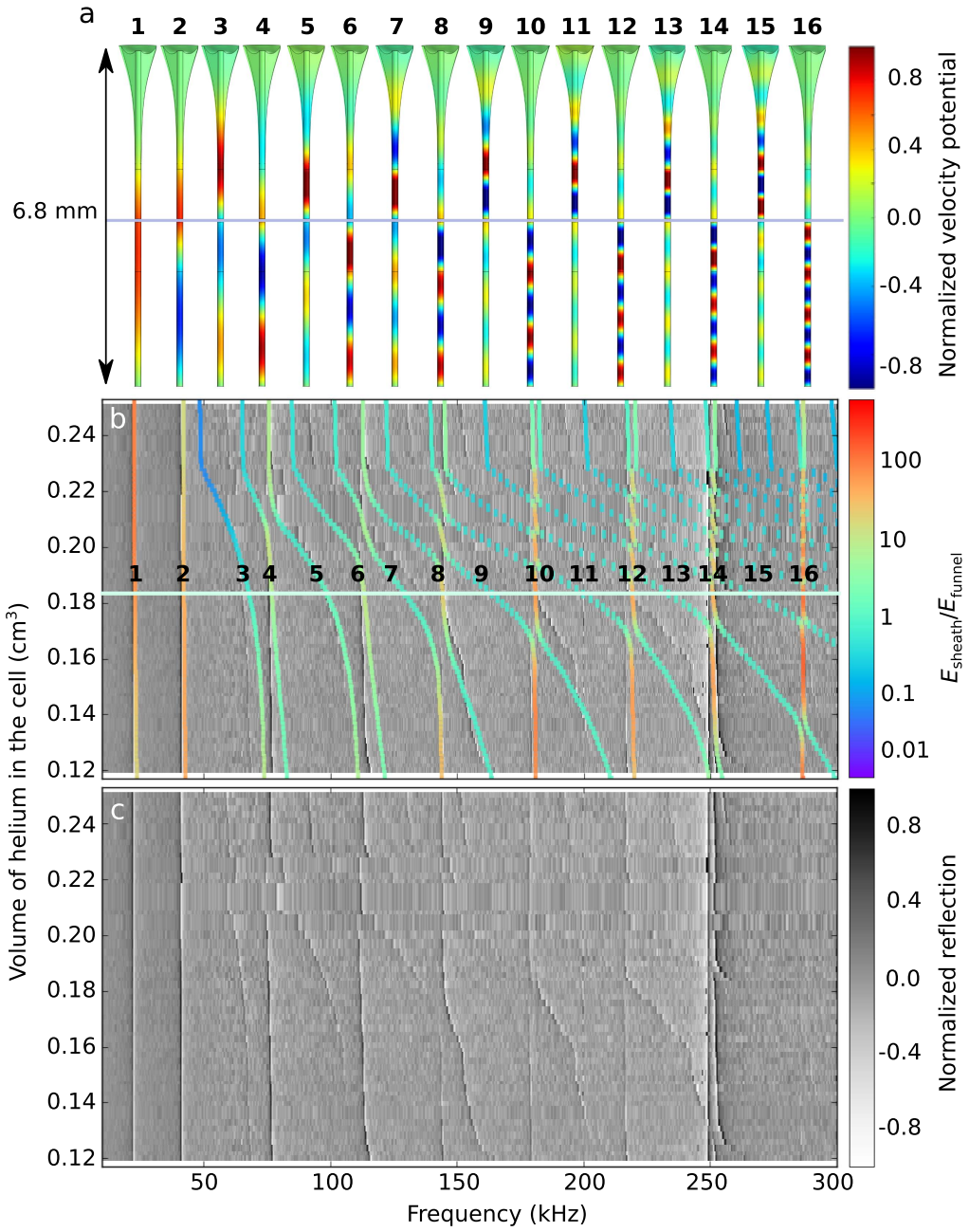

Figure 4. The ferrule modes. (a) Several mode profiles of the helium in the ferrule when the helium level is 6.8 mm, calculated using COMSOL. The color indicates the normalized velocity potential. Some of the modes (e.g. 10,12,14,16) are mostly localized in the sheath of helium surrounding the fibers in the bore below the cavity. Some other modes (e.g. 9,11,13,15) are mostly localized in the helium above the cavity. The gray line shows the position of the cavity. (b) Solid lines: the frequencies of the modes as a function of the volume of helium accumulated in the device. The color indicates the ratio of energy stored in the sheath to the energy stored in the funnel. The modes that are mostly confined in the sheath do not change in frequency as the more helium accumulates in the cell. The modes that extend into the funnel show a decrease in frequency as the helium level rises. The light blue line is at 0.182 cm^3 (which corresponds to 6.8 mm of helium in the ferrule and hence the simulations is panel (a)). The black numbers are located at the intersections of the light blue line with the colored lines correspond to the numbers in panel (a). Density plot: the measurements also shown in (c). (c) Density plot of the OMIT/OMIA signal for intracavity beatnote frequencies in range 10–300 kHz as a function of the volume of helium condensed in the device.

Here, $K = v^2\rho$ is the bulk modulus, v is the speed of sound.

To calculate the single photon coupling g_0, we equate E_1 to the energy stored in a zero point fluctuation:

$$E_0 = \frac{\hbar\omega_m}{4}. \tag{25}$$

Combining equations (24) and (25), we solve for the normalization constant ϵ_1:

$$\epsilon_1 = \sqrt{\frac{\hbar\omega_m}{2v^2\rho\int_V p(\vec{r})^2 \mathrm{d}^3\vec{r}}}. \tag{26}$$

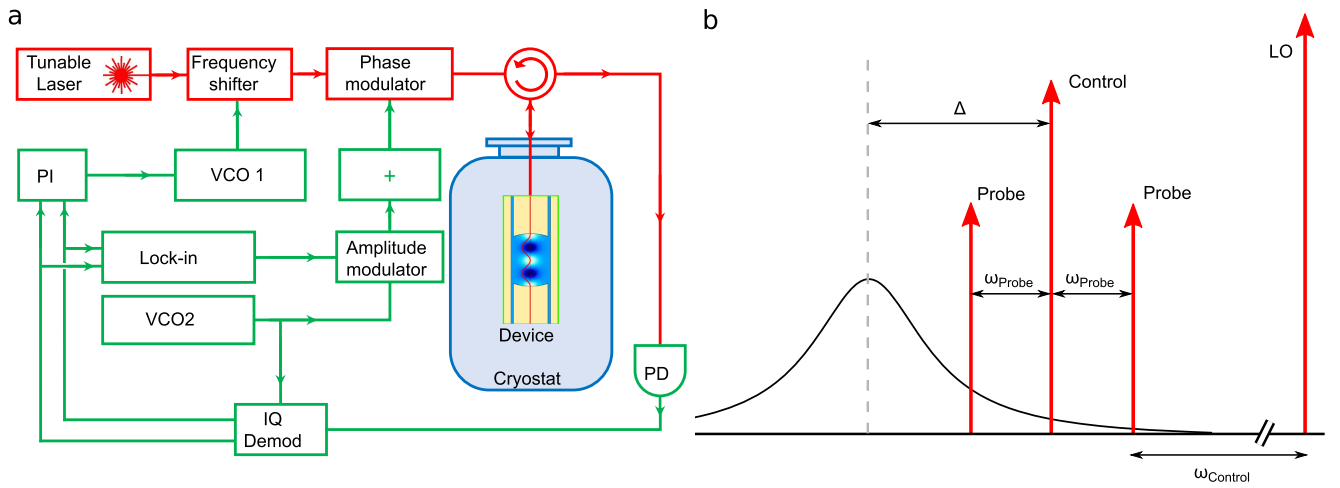

Figure 5. The measurement setup. (a) Schematic of the measurement setup. The optical components are shown in red, electronic components are shown in green. For detailed description see section 5. (b) Illustration of the laser beams incident on the cavity. The LO, control, and both probe beams are shown (red), along with the cavity resonance (black).

Using equation (26), the electrostrictive single phonon coupling can be calculated from equation (23), given the optical and acoustic mode profiles.

The calculated values of electrostrictive coupling to the radial modes with $m = 0$ (red circles) and $m = 1$ (blue triangles) versus the frequencies of the modes obtained using equation (18) are shown in figure 3(a). The faint solid lines show the electrostrictive coupling in the case of the optical mode being aligned perfectly with the axis of the cylinder (optical intensity described by equation (15)). The bright solid lines show the coupling for the case of optical mode being offset from the axis of the cylinder by 3 μm (optical intensity described by equation (16)). As can be seen from figure 3(a), the misalignment results in coupling to $m = 1$ mode.

5. Measurement setup and fits to the data

The measurement setup is shown in figure 5(a). The light leaves a tunable laser and passes through a frequency shifter. The frequency shifter is used to lock the laser frequency to the experimental cavity, as described below. The light then passes through a phase modulator. The phase modulator is used to add three pairs of sidebands: a control beam generated by a Voltage Controlled Oscillator (VCO2) at $\omega_{\text{control}} = 2\pi \times 926$ MHz and two probe beams, which are AM sidebands of the control beam and are generated by a microwave amplitude modulator driven at a frequency ω_{probe} by a lock-in. The carrier beam serves as a local oscillator (LO). The light is delivered to and returned from the cryostat via an optical circulator. Returning light lands on a photodiode. The photocurrent has beatnotes at ω_{control} as well as at $\omega_{\text{control}} \pm \omega_{\text{probe}}$. The photocurrent is sent into an IQ demodulator, where it is demodulated at ω_{control}. Both quadratures on the output of the IQ demodulator have a DC component which carries information about the offset of the control beam from the cavity, and a component at frequency ω_{probe}, which carries information about the upper and lower sidebands generated by the motion of the acoustic mode. The DC component is then used to generate a feedback signal to control the frequency shifter via VCO1. Additionally, both quadratures are sent into the lock-in and demodulated at ω_{probe} to gain information about the acoustic response at that frequency. For the OMIT measurements the frequency ω_{probe} is swept through the resonant frequency of the acoustic mode of interest. Examples of these measurements are shown in figures 6(a) and (b).

The data obtained in the manner described above are fit to extract the linewidth and frequency of the acoustic modes, as well the amplitude and phase of the OMIT/OMIA response. All those quantities are fit simultaneously with the OMIT/OMIA theory [1, 17] to extract the electrostrictive and photothermal coupling. Since the amplitude modulation scheme is employed, the theory described in [1] needs to be modified to include the second probe beam. This modification is described below.

5.1. OMIT/OMIA theory with two probe beams

We start the derivation with the expressions for the optical and acoustic amplitudes $\delta\hat{a}[\omega]$ and $\delta\hat{b}[\omega]$ derived in [1]:

$$\delta\hat{a}[\omega] = -i\chi_{\text{cav}}[\omega](g(\delta\hat{b}[\omega] + \delta\hat{b}^{\dagger}[\omega]) + \sqrt{\kappa_{\text{in}}}\delta s_{\text{in}}[\omega]), \tag{27}$$

$$\delta\hat{b}[\omega] = \frac{G\sqrt{\kappa_{\text{in}}}(\chi^{*}_{\text{cav}}[-\omega]\delta s^{*}_{\text{in}}[\omega]g - \chi_{\text{cav}}[\omega]\delta s_{\text{in}}[\omega]g^{*})}{-i(\omega - \omega_m) + \frac{\gamma_m}{2} + i\Sigma[\omega]}. \tag{28}$$

Here κ_{in} is the input coupling, $\delta s[\omega]$ is the amplitude of a probe beam at frequency ω away from the control beam, g is the multiphoton electrostrictive coupling defined as:

$$g = g_0\frac{-i\sqrt{\kappa}_{\text{in}}s_{\text{in}}}{-i\bar{\Delta} + \frac{\kappa}{2}}. \tag{29}$$

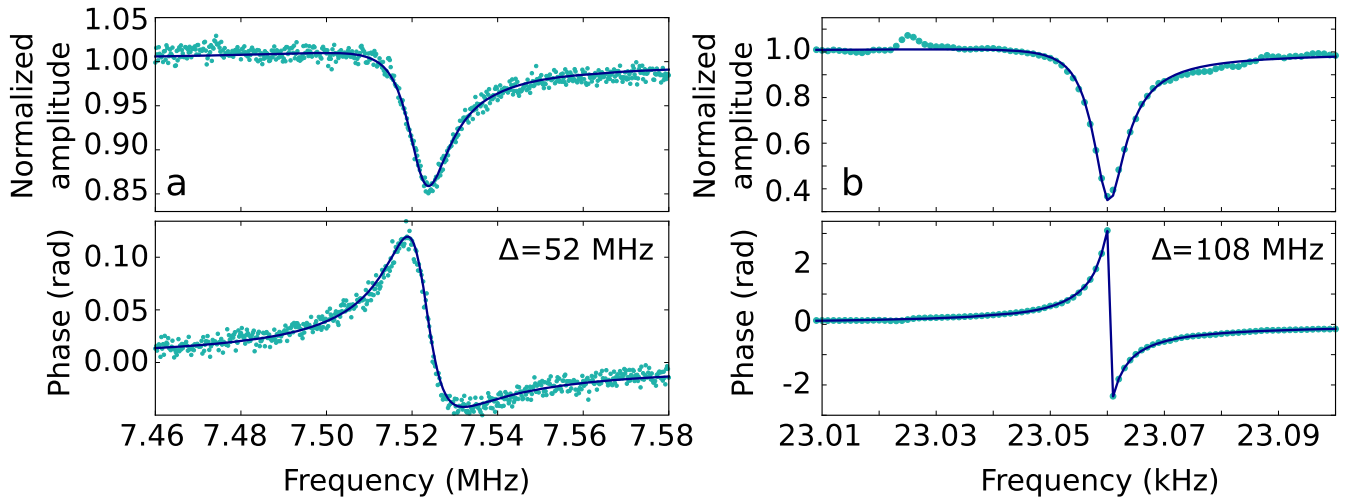

Figure 6. OMIT measurements. The teal points are the normalized amplitude (a) and phase (ψ) of the OMIT signal as a function of the intracavity beat note frequency $|\omega_{\text{control}} - \omega_{\text{probe}}|/2\pi$. The data is taken by sweeping the frequency difference between the control and probe beams. Shown are the sweeps of the probe beam, which is blue-detuned from the control beam. The data is normalized so that far from the resonance $a = 1$ and $\psi = 0$. The solid blue line is fit to a complex Lorentzian. The fit parameters are A_+ and Ψ_+ (the overall amplitude and phase of the OMIT effect), ω_m (the acoustic frequency), and γ_m (the acoustic damping rate). (a) The sweep over one of the radial modes. The intracavity beat note frequency is varied between 7.46 and 7.58 MHz. The control beam is detuned from the cavity resonance by 52 MHz. (b) The sweep over one of the ferrule modes. The intracavity beat note frequency is varied between 23.0 and 23.1 kHz. The control beam is detuned from the cavity resonance by 108 MHz.

$\chi_{\text{cav}}[\omega]$ is the cavity susceptibility at frequency ω defined as:

$$\chi_{\text{cav}}[\omega] = \frac{1}{-\mathrm{i}\omega - \mathrm{i}\bar{\Delta} + \frac{\kappa}{2}}. \tag{30}$$

$\bar{\Delta}$ is the effective detuning of control beam from the cavity and s_{in} is the amplitude of the control beam. $\Sigma[\omega]$ is optomechanical self-energy defined as:

$$\mathrm{i}\Sigma[\omega] = G|g|^2(\chi_{\text{cav}}[\omega] - \chi^*_{\text{cav}}[-\omega]). \tag{31}$$

The G is derived in [1] and defined as:

$$G = 1 + \frac{g_1}{g_0}\frac{1}{1 - \mathrm{i}\omega/\kappa_{\text{Th}}} = 1 + \frac{g_{1,\text{filt}}}{g_0}, \tag{32}$$

where we now define a complex quantity:

$$g_{1,\text{filt}} = \frac{g_1}{1 - \mathrm{i}\omega/\kappa_{\text{Th}}}. \tag{33}$$

The second term in the definition of G is due to the photothermal coupling. The photothermal force has coupling strength g_1; κ_{Th} is photothermal bandwidth which is inversely proportional to the relaxation time for the photothermal process. The complex quantity $g_{1,\text{filt}}$ represents the photothermal coupling, as filtered by the photothermal bandwidth.

The optical spring and damping are then defined as:

$$\Delta\omega_{m\,(\text{opt})} = \text{Re}[\Sigma[\omega]] \quad \text{and} \quad \gamma_{m\,(\text{opt})} = -2\,\text{Im}[\Sigma[\omega]]. \tag{34}$$

Since an amplitude modulation scheme is employed, the laser has two sidebands: at positive and negative Ω. The expression for $\delta s_{\text{in}}(t)$ is:

$$\delta s_{\text{in}}(t) = s_{\text{p}}(\mathrm{e}^{-\mathrm{i}\Omega t} + \mathrm{e}^{\mathrm{i}\Omega t}). \tag{35}$$

Taking the Fourier transform and assuming s_p is real:

$$\delta s_{\text{in}}[\omega] = \delta s^*_{\text{in}}[\omega] = \sqrt{2\pi}\, s_{\text{p}}(\delta(\omega - \Omega) + \delta(\omega + \Omega)). \tag{36}$$

Putting this back into the equation (28):

$$\delta\hat{b}[\omega] = \frac{\sqrt{2\pi}\, s_{\text{p}} G\sqrt{\kappa_{\text{in}}}\,(\chi^*_{\text{cav}}[-\omega]g - \chi_{\text{cav}}[\omega]g^*)(\delta(\omega - \Omega) + \delta(\omega + \Omega))}{-\mathrm{i}(\omega - \omega_m) + \frac{\gamma_m}{2} + \mathrm{i}\Sigma[\omega]}. \tag{37}$$

In the time domain:

$$\delta\hat{b}(t) = b_+[\Omega]s_{\text{p}}\mathrm{e}^{-\mathrm{i}\Omega t} + b_-[\Omega]s_{\text{p}}\mathrm{e}^{\mathrm{i}\Omega t}, \tag{38}$$

where

$$b_+[\Omega] = \frac{G\sqrt{\kappa_{\text{in}}}\,(\chi^*_{\text{cav}}[-\Omega]g - \chi_{\text{cav}}[\Omega]g^*)}{-\mathrm{i}(\Omega - \omega_m) + \frac{\gamma_m}{2} + \mathrm{i}\Sigma[\Omega]} \tag{39}$$

and

$$b_-[\Omega] = \frac{G\sqrt{\kappa_{\text{in}}}\,(\chi^*_{\text{cav}}[\Omega]g - \chi_{\text{cav}}[-\Omega]g^*)}{-\mathrm{i}(-\Omega - \omega_m) + \frac{\gamma_m}{2} + \mathrm{i}\Sigma[-\Omega]}. \tag{40}$$

The expression for b_+ gives us the motion of the acoustic oscillator; b_- oscillates at $-\Omega$, and so is far off resonance and therefore small. Writing the acoustic mode amplitude in the time domain and neglecting b_- yields:

$$g(\delta\hat{b}(t) + \delta\hat{b}^{\dagger}(t)) + \sqrt{\kappa_{\rm in}}\delta s_{\rm in}(t) = ((gb_{+}[\Omega] + \sqrt{\kappa_{\rm in}})e^{-i\Omega t} + (gb_{+}^{*}[\Omega] + \sqrt{\kappa_{\rm in}})e^{i\Omega t})s_{\rm p}. \quad (41)$$

Combining equations (27) and (41), we express the cavity mode amplitude as:

$$\delta\hat{a}(t) = a_{+}[\Omega]e^{-i\Omega t} + a_{-}[\Omega]e^{i\Omega t}, \quad (42)$$

where

$$a_{+}[\Omega] = -i\chi_{\rm cav}[\Omega](gb_{+}[\Omega] + \sqrt{\kappa_{\rm in}})s_{\rm p}$$
$$\text{and} \quad a_{-}[\Omega] = -i\chi_{\rm cav}[-\Omega](gb_{+}^{*}[\Omega] + \sqrt{\kappa_{\rm in}})s_{\rm p}. \quad (43)$$

The expression for a_- gives the signal measured at the lower probe beam frequency and the expression for a_+ gives the signal measured at the upper probe beam frequency. In figures 6(a) and (b), we plot one of the sidebands a_+ normalized with respect to the background. The normalized signals a_-' and a_+' are given by:

$$a_{-}'[\Omega] = \frac{a_{-}[\Omega]}{a_{-}[\infty]} = \frac{gb_{+}^{*}[\Omega]}{\sqrt{\kappa_{\rm in}}} + 1$$
$$\text{and} \quad a_{+}'[\Omega] = \frac{a_{+}[\Omega]}{a_{+}[\infty]} = \frac{gb_{+}[\Omega]}{\sqrt{\kappa_{\rm in}}} + 1. \quad (44)$$

The normalized signals a_-' and a_+' have Lorentzian shape. The values of amplitude (A_+) and phase (Ψ_+) of the OMIT/OMIA response at the upper probe beam frequency are defined as the magnitude and phase of $a_+'[\omega_m] - 1$, and the values of amplitude (A_-) and phase (Ψ_-) of the OMIT/OMIA response at the lower probe beam frequency are defined as the magnitude and phase of $a_-'[-\omega_m] - 1$.

6. Results and discussion

In figure 3(b) the thick black line shows a typical measurement of the OMIT/OMIA response for the intracavity beatnote frequency in the range 1–20 MHz. The sharp features are the radial modes. The dashed lines are the predicted frequencies for the radial indices $m = 0$ (red) and $m = 1$ (blue), obtained using COMSOL simulations. The frequencies obtained from COMSOL show good agreement with the frequencies calculated using an analytical expression shown in figure 3(a) and with the frequencies obtained experimentally. The features associated with the $m = 0$ modes are dominant, but there is also clearly coupling to the $m = 1$ modes, which confirms that the optical mode is not perfectly aligned with the axis of the cylinder.

Figures 4(b) and (c) shows a density plot of the OMIT/OMIA response for intracavity beatnote frequencies in the range 20–300 kHz (the frequency range of the ferrule modes). The vertical axis is the amount of helium accumulated in the device.

Figure 4(b) additionally shows the overlaid COMSOL simulation of the frequencies of the modes. In order for the data to agree with the COMSOL simulations, we need to take the volume of the helium film to be $V_{\rm film} = 0.22\ {\rm cm}^3$, which is within the predicted bounds. The rate at which helium accumulates in the device is found to be $\dot{V} = 6.5 \times 10^{-4}$ ${\rm cm}^3\,{\rm min}^{-1}$, which is larger than the original prediction of 4×10^{-4} ${\rm cm}^3\,{\rm min}^{-1}$, obtained using equation (1). The discrepancy can be attributed to the roughness of the inner surface of the capillary, which increases its surface area.

In order to understand the optomechanical coupling to the modes, we measured the OMIT/OMIA feature for the 7.5 MHz radial mode and the 23 kHz ferrule mode. These modes clearly showed the familiar optical spring and optical damping [27], however the sign and relative magnitude of these effects were inconsistent with coupling via electrostriction. Figure 7 shows the linewidth, frequency, amplitude, and phase of the OMIT feature relative to the background as a function of the control beam detuning for the 7.5 MHz mode. The data is fit with the OMIT/OMIA theory described in section 6, using the theoretical value of electrostrictive coupling $g_0 \simeq 2\pi \times 300$ Hz (calculated from equation (23)) and assuming the acoustic mode profile $p(r, \theta) = J_0(\alpha_{05} r/R)$. From this fit, we extract the intrinsic linewidth of the mode to be 11.7 kHz (corresponding to a quality factor $Q = 642$), and $\kappa_{\rm Th} = 2\pi \times 1.1 \pm 0.2$ MHz

Figure 8 shows the corresponding measurements for the 23 kHz ferrule mode. The intrinsic linewidth of this mode is 19 Hz, corresponding to a quality factor $Q = 1,200$. The value of electrostrictive coupling to the ferrule modes is not known *a priori*, so the fits are underconstrained. However large values of $\kappa_{\rm Th}$ result in almost perfect cancellation of g_1 and g_0. For example, for $\kappa_{\rm Th} > 2\pi \times 30$ kHz, the ratio $|g_1/g_0 + 1| < 0.05$. Since there is no physical mechanism that would cause the coupling rates to almost cancel, we limit $\kappa_{\rm Th} < 2\pi \times 30$ kHz. This allows us to put bounds on g_0 to be between $2\pi \times 230$ Hz and $2\pi \times 600$ Hz.

The findings are summarized in table 1, where the real and imaginary parts of $g_{\rm l,filt}$ are calculated as well to ease the comparison with [1].

We note that for the paraxial mode, studied in [1], we used the assumption that the photothermal bandwidth is much smaller than the driving frequency, which allowed us to set the real part of $g_{\rm l,filt}$ to zero. This assumption was justified for the large driving frequency $\omega_m \simeq 317$ MHz. We are not making the same assumption for the modes studied here, which allows us to extract the value of $\kappa_{\rm Th}$. We note that $\kappa_{\rm Th}$ differs greatly between ferrule and radial modes, from which we can infer that there are at least two different photothermal coupling mechanisms.

The photothermal coupling to the 23 kHz ferrule mode could result from helium counterflow [28, 29]. Although the device operates at temperatures where the simple two-fluid model is not valid, we note that thermal phonons radiated from the mirror hot spot will result in a net transport of

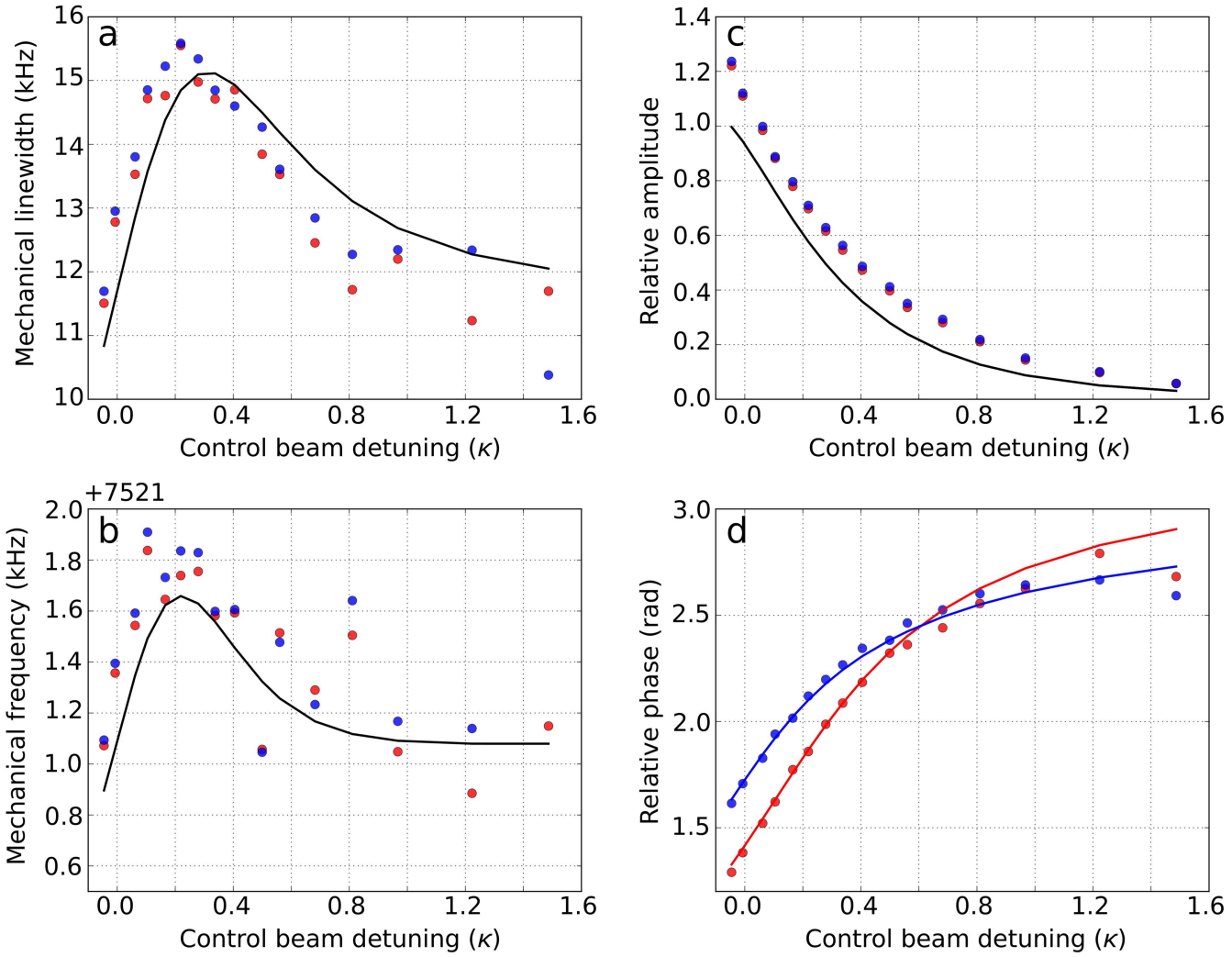

Figure 7. Optomechanical effects for the 7.5 MHz radial mode. Plotted with blue (red) points are the values of the fit parameters for the OMIT/OMIA response at upper (lower) probe beam frequencies extracted from data sweeps such as shown in figure 6(a) for various detunings of the control beam. The power in the control beam is 0.6 μW. The horizontal axis is the detuning of the control beam from the cavity in units of κ. The solid lines are the fits discussed in the text, using the measured values of κ, $\kappa_{\rm in}$, $s_{\rm in}$ and $\bar{\Delta}$. The fits to the acoustic linewidth, acoustic frequency, amplitude and phase of the OMIT/OMIT response relative to the background are all done simultaneously, assuming the theoretical value of electrostrictive coupling $g_0 = 2\pi \times 300$ Hz. The values of $\kappa_{\rm Th} = 2\pi \times 1.1 \pm 0.2$ MHz, as well as the the intrinsic linewidth $\gamma_m = 2\pi \times 11.7$ kHz and the intrinsic frequency $\omega_m = 2\pi \times 7.52$ MHz are the fit parameters extracted from the fit. (a) The acoustic linewidth. The solid line is the fit to: $(\gamma_m + \gamma_{m(\rm opt)})/2\pi$. (b) The acoustic frequency. The solid line is the fit to: $(\omega_m + \Delta\omega_{m(\rm opt)})/2\pi$. (c) The amplitude of the OMIT/OMIA response relative to the background. The solid line is the fit to A_+ and A_- which are the same in the case of amplitude modulation. (d) The phase of the OMIT/OMIA response relative to the background. The solid blue (red) line is the fit to Ψ_+ (Ψ_-).

helium, which must be balanced by the flow of superfluid towards the hot spot. This can lead to optomechanical coupling in the following way: scattering may prevent the thermal phonons from traveling efficiently through the thin sheath between the ferrule and the fiber, while the superfluid component travels easily through this sheath. This can create a temporary imbalance in which more helium is accumulated close to the hot mirrors, thereby driving the acoustic mode. The bandwidth for this effect is set by the thermal equilibration time inside the cavity, which was measured in [1] to be $\tau \approx 350$ μs, corresponding to bandwidth of 0.5kHz, which is consistent with the range of $\kappa_{\rm Th}$ found for this mode ($<2\pi \times 30$ kHz).

The photothermal coupling to the 7.5 MHz radial mode can be explained in terms of the thermal expansion of the fiber mirrors due to laser heating. This expansion moves the glass/LHe boundary, and so drives the acoustic mode. The value of $\kappa_{\rm Th}$ found for this mode ($2\pi \times 1.1 \pm 0.2$ MHz) is consistent with the results of [30], where the bandwidth for the expansion of similar mirrors was measured at room temperature. The rough agreement between our results (for which $T < 1$ K) and the room temperature results of [30] may

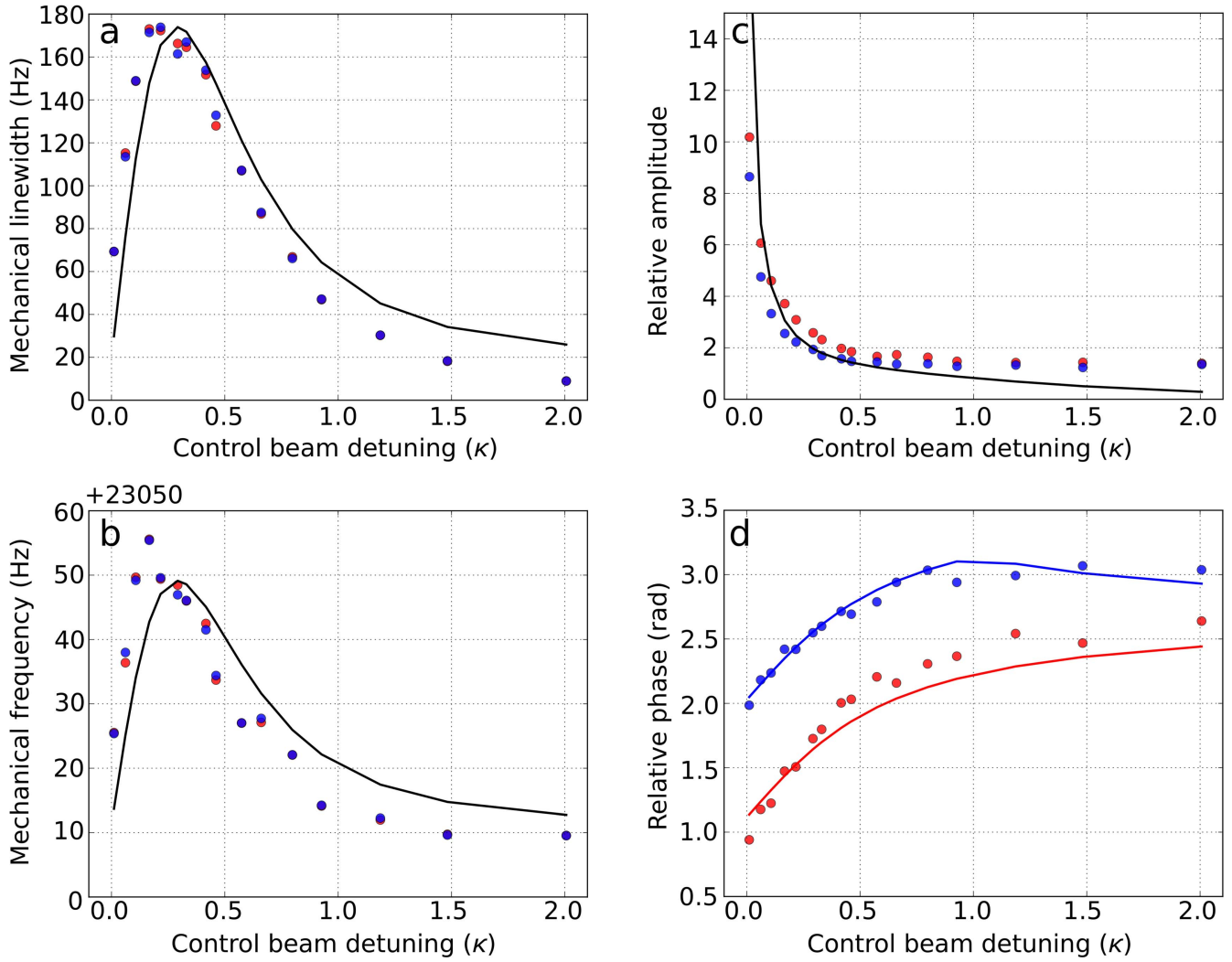

Figure 8. Optomechanical effects for the 23 kHz ferrule mode. Plotted with blue (red) points are the values of the fit parameters for the OMIT/OMIA response at upper (lower) probe beam frequencies extracted from data sweeps such as shown in figure 6(b) for various detunings of the control beam. The power in the control beam is 0.6 μW. The detuning of the control beam is plotted on the x-axis in units of κ. The solid lines are the theory fits, using the measured values of κ, $\kappa_{\rm in}$, $s_{\rm in}$ and $\bar{\Delta}$. The fits to the acoustic linewidth, acoustic frequency, amplitude and phase of the OMIT/OMIA response relative to the background are all done simultaneously. The intrinsic linewidth $\gamma_m = 2\pi \times 19$ Hz and the intrinsic frequency $\omega_m = 2\pi \times 23.061$ kHz are the fit parameters extracted from the fit. Additionally the value of $\kappa_{\rm Th}$ is less than $2\pi \times 30$ kHz and the electrostrictive coupling rate g_0 is between $2\pi \times 230$ Hz and $2\pi \times 600$ Hz as described in the text. (a) The acoustic linewidth. The solid line is the fit to: $(\gamma_m + \gamma_{m\,(\rm opt)})/2\pi$. (b) The acoustic frequency. The solid line is the fit to: $(\omega_m + \Delta\omega_{m\,(\rm opt)})/2\pi$. (c) The amplitude of the OMIT/OMIA response relative to the background. The solid line is the fit to A_+ and A_- which are the same in the case of amplitude modulation. (d) The phase of the OMIT/OMIA response relative to the background. The solid blue (red) line is the fit to Ψ_+ (Ψ_-).

Table 1. Properties of the two types of mode (ferrule and radial) studied here, as well as the corresponding properties of the paraxial modes studied in [1].

Mode	$\omega_m/(2\pi)$	$g_0/(2\pi)$	$\kappa_{\rm Th}/(2\pi)$	${\rm Re}[g_{\rm 1,filt}]/(2\pi)$	${\rm Im}[g_{\rm 1,filt}]/(2\pi)$
Ferrule	23 kHz	0.23 ∼ 0.6 kHz	<30 kHz	0 ∼ −0.5 kHz	−0.5 ∼ −0.16 kHz
Radial	7.5 MHz	0.3 kHz	1.1 ± 0.2 MHz	−1.1 ± 0.4 kHz	−7.5 ± 1.7 kHz
Paraxial	317 MHz	3.18 ± 0.2 kHz	≪317 MHz	set to 0 Hz	0.97 ± 0.05 kHz

reflect an approximate cancellation of the temperature dependence of thermal conductivities and heat capacities for the relevant materials.

While both mechanisms are always present in the system, our analysis assumes that one of them dominates for each mode family. This makes sense intuitively: the counterflow

mechanism results in larger helium density in the region between the fibers but with little variation within that region, and so should not couple efficiently to the radial modes. Additionally, the bandwidth of the counterflow mechanism is low, so the coupling of this mechanism to the radial modes is strongly filtered. In contrast, the expansion mechanism couples efficiently to modes whose wavelength is on the order of the hot spot ($\approx$10 μm), resulting in stronger coupling to radial modes.

7. Conclusion

We have studied two families of acoustic modes that exist in a superfluid-filled optical cavity. In contrast to [1], these families are associated with the overall geometry of the device and its surroundings, rather than the with the cavity's paraxial modes. The frequencies of the modes and their dependence on the amount of helium added to the cell were understood. Additionally, the modes' optical spring and optical damping were measured, and these results were analyzed using a model that includes an instantaneous electrostricitve coupling as well as a non-instantaneous photothermal coupling. Both types of mode show a significant photothermal coupling. However they show widely divergent time scales for this coupling. We attribute this to the presence of two different microscopic mechanisms for photothermal coupling in this system. The first is the thermal expansion of the materials confining the superfluid. The second is the different rate of mass transport via superfluid flow and thermal excitations. These two mechanisms are associated with different time scales and also with different spatial profiles, which tends to ensure that each one couples to only one type of acoustic mode. These results highlight the wide range of microscopic mechanisms that can give rise to optomechanical coupling [27, 31, 32] and provide insight into the behavior of superfluid-filled optical cavities

Acknowledgments

We are grateful to Vincent Bernardo, Joe Chadwick, John Cummings, Andreas Fragner, Glen Harris, Katherine Lawrence, Donghun Lee, Daniel McKinsey, Peter Rakich, Robert Schoelkopf, Hong Tang, Jedidiah Thompson, and Zuyu Zhao for their assistance. We acknowledge financial support from W M Keck Foundation Grant No. DT121914, AFOSR Grants FA9550-09-1-0484 and FA9550-15-1-0270, DARPA Grant W911NF-14-1-0354, ARO Grant W911NF-13-1-0104, and NSF Grant 1205861. This work has been supported by the DARPA/MTO ORCHID program through a grant from AFOSR. This project was made possible through the support of a grant from the John Templeton Foundation. The opinions expressed in this publication are those of the authors and do not necessarily reflect the views of the John Templeton Foundation. This material is based upon work supported by the National Science Foundation Graduate Research Fellowship under Grant No. DGE-1122492. LH, KO and JR acknowledge funding from the EU Information and Communication Technologies program (QIBEC project, GA 284584), ERC (EQUEMI project, GA 671133), and IFRAF.

References

[1] Kashkanova A D, Shkarin A B, Brown C D, Flowers-Jacobs N E, Childress L, Hoch S W, Hohmann L, Ott K, Reichel J and Harris J G E 2016 Superfluid Brillouin optomechanics *Nat. Phys.* (https://doi.org/10.1038/nphys3900)

[2] Bahl G, Kim K H, Lee W, Liu J, Fan X and Carmon T 2013 Brillouin cavity optomechanics with microfluidic devices *Nat. Commun.* **4** 1994

[3] Kim K H, Bahl G, Lee W, Liu J, Tomes M, Fan X and Carmon T 2013 Cavity optomechanics on a microfluidic resonator with water and viscous liquids *Light Sci. Appl.* **2** e110

[4] Sun X, Zhang X, Schuck C and Tang H X 2013 Nonlinear optical effects of ultrahigh-Q silicon photonic nanocavities immersed in superfluid helium *Sci. Rep.* **3** 1436

[5] Colgate S O, Sivaraman A, Dejsupa C and McGill K C 1991 Acoustic cavity method for phase boundary determinations: the critical temperature of CO_2 *Rev. Sci. Instrum.* **62** 198

[6] Harris G I, Mcauslan D L, Sheridan E, Sachkou Y, Baker C and Bowen W P 2016 Laser cooling and control of excitations in superfluid helium *Nat. Phys.* **12** 788–93

[7] Gil-Santos E, Baker C, Nguyen D T, Hease W, Gomez C, Lemaître A, Ducci S, Leo G and Favero I 2015 High-frequency nano-optomechanical disk resonators in liquids *Nat. Nanotechnol.* **10** 810–6

[8] DeLorenzo L A and Schwab K C 2014 Superfluid optomechanics: coupling of a superfluid to a superconducting condensate *New J. Phys.* **16** 113020

[9] Seidel G M, Lanou R E and Yao W 2002 Rayleigh scattering in rare-gas liquids *Nucl. Instrum. Methods Phys. Res.* A **489** 189–94

[10] Greywall D 1981 Thermal-conductivity measurements in liquid ^{4}He below 0.7 K *Phys. Rev.* B **23** 2152–68

[11] Abraham B M, Eckstein Y, Ketterson J B, Kuchnir M and Vignos J 1969 Sound propagation in liquid ^{4}He *Phys. Rev.* **181** 347–73

[12] Flowers-Jacobs N E, Hoch S W, Sankey J C, Kashkanova A, Jayich A M, Deutsch C, Reichel J and Harris J G E 2012 Fiber-cavity-based optomechanical device *Appl. Phys. Lett.* **101** 221109

[13] Hunger D, Deutsch C, Barbour R J, Warburton R J and Reichel J 2012 Laser micro-fabrication of concave, low-roughness features in silica *AIP Adv.* **2** 012119

[14] Hunger D, Steinmetz T, Colombe Y, Deutsch C, Hänsch T W and Reichel J 2010 A fiber Fabry–Perot cavity with high finesse *New J. Phys.* **12** 065038

[15] Rempe G, Lalezari R, Thompson R J and Kimble H J 1992 Measurement of ultralow losses in an optical interferometer *Opt. Lett.* **17** 363–5

[16] Donnelly R J and Barenghi C F 1998 The observed properties of liquid helium at the saturated vapour pressure *J. Phys. Chem. Ref. Data* **27** 1217

[17] Weis S, Rivière R, Deléglise S, Gavartin E, Arcizet O, Schliesser A and Kippenberg T J 2010 Optomechanically induced transparency *Science* **330** 1520–3

[18] Rollin B V and Simon F 1939 On the 'film' phenomenon of liquid helium II *Physica* **6** 219–30

[19] Pobell F 2007 *Matter and Methods at Low Temperatures* (Berlin: Springer)

[20] Franco H, Bossy J and Godfrin H 1984 Properties of sintered silver powders and their application in heat exchangers at millikelvin temperatures *Cryogenics* **24** 477–83
[21] Wang Z, Chang C C, Hong S J, Sheng Y J and Tsao H K 2012 Capillary rise in a microchannel of arbitrary shape and wettability: hysteresis loop *Langmuir* **28** 16917–26
[22] Eckardt J R, Edwards D O, Shen S Y and Gasparini F M 1977 Surface tension and surface entropy of superfluid ^{4}He *Phys. Rev.* B **16** 1944–53
[23] Pozrikidis C 2009 *Fluid Dynamics: Theory, Computation, and Numerical Simulation* (New York: Oxford University Press)
[24] Siegman A E 1986 *Lasers* (Mill Valley, CA: University Science Books)
[25] Jackson J D 1999 *Classical Electrodynamics* 3rd edn (New York: Wiley)
[26] Abraham B M, Eckstein Y, Ketterson J B, Kuchnir M and Roach P R 1970 Velocity of sound, density, and Gruneisen constant in liquid ^{4}He *Phys. Rev.* A **1** 250–7
[27] Aspelmeyer M, Kippenberg T J and Marquardt F 2014 Cavity optomechanics *Rev. Mod. Phys.* **86** 1391
[28] Roberts P H and Donnelly R J 1974 Superfluid mechanics *Annu. Rev. Fluid Mech.* **6** 179–225
[29] Mcauslan D L, Harris G I, Baker C, Sachkou Y, He X, Sheridan E and Bowen W P 2016 Microphotonic forces from superfluid flow *Phys. Rev.* X **6** 021012
[30] Brachmann J F S, Haupp H, Hansch T W and Hunger D 2016 Photothermal effects in ultra-precisely stabilized tunable microcavities *Opt. Express* **24** 12813–20
[31] Florez O, Jarschel P F, Espinel Y A V, Cordeiro C M B, Mayer Alegre T P, Wiederhecker G S and Dainese P 2016 Brillouin scattering self-cancellation *Nat. Commun.* **7** 11759
[32] Butsch A, Koehler J R, Noskov R E and Russell P S J 2014 CW-pumped single-pass frequency comb generation by resonant optomechanical nonlinearity in dual-nanoweb fiber *Optica* **1** 158–64